High-rate nanofluidic energy absorption in porous zeolitic frameworks

Sun, Yueting; Rogge, Sven M. J.; Lamaire, Aran; Vandenbrande, Steven; Wieme, Jelle; Siviour, Clive R.; Speybroeck, Veronique Van; Tan, Jin-Chong

DOI:
10.1038/s41563-021-00977-6

High rate nanofluidic energy absorption in porous zeolitic frameworks

Yueting Sun[1,3†*], Sven M.J. Rogge[2†*], Aran Lamaire[2], Steven Vandenbrande[2], Jelle Wieme[2], Clive R. Siviour[1], Veronique Van Speybroeck[2*], Jin-Chong Tan[1*]

[1]Department of Engineering Science, University of Oxford, Parks Road, Oxford OX1 3PJ, United Kingdom.

[2]Center for Molecular Modeling (CMM), Ghent University, Technologiepark 46, 9052 Zwijnaarde, Belgium.

[3]School of Engineering, University of Birmingham, Edgbaston, Birmingham B15 2TT, United Kingdom.

[†]These authors contributed equally to this work

*Corresponding authors: Y.Sun.9@bham.ac.uk ; Sven.Rogge@UGent.be ; Veronique.VanSpeybroeck@UGent.be ; jin-chong.tan@eng.ox.ac.uk

Abstract

Optimal mechanical impact absorbers are reusable and exhibit high specific energy absorption. The forced intrusion of liquid water in hydrophobic nanoporous materials, such as zeolitic imidazolate frameworks (ZIFs), presents an attractive pathway to engineer such systems. However, to harness their full potential, it is crucial to understand the underlying water intrusion and extrusion mechanisms under realistic, high-rate deformation conditions. Herein, we report a critical increase of the energy absorption capacity of confined water-ZIF systems at elevated strain rates. Starting from ZIF-8 as proof-of-concept, we demonstrate that this attractive rate dependence is generally applicable to cage-type ZIFs but disappears for channel-containing zeolites. Molecular simulations reveal that this phenomenon originates from the intrinsic nanosecond timescale needed for critical-sized water clusters to nucleate inside the nanocages, expediting water transport through the framework. Harnessing this fundamental understanding, design rules are formulated to construct effective, tailorable, and reusable impact energy absorbers for challenging new applications.

Energy absorption during mechanical impact plays a crucial role in modern society, from injury prevention and safety measures in industrial settings to cushioning systems that increase user comfort.[1] As current state-of-the-art energy absorption materials rely on processes such as extensive plastic deformation, cell buckling, and viscoelastic dissipation,[2,3] a major dilemma is the conflict between the required high energy density and the desire for reusability, to afford protection from multiple impacts. This challenge motivates the development of efficient energy absorbing systems that are intrinsically recoverable, which requires one to identify and leverage fundamentally new energy absorption mechanisms.

In this regard, the pressurized intrusion of liquid water and aqueous solutions in hydrophobic nanoporous materials such as zeolites and metal-organic frameworks (MOFs) has emerged as a promising mechanism to yield high-performance energy absorbing systems.[4-6] In this process, a hydrostatic pressure forces water to intrude into the hydrophobic nanopores, thereby converting mechanical work into interfacial energy. Given the exceedingly large surface area of MOFs (typically 1,000-10,000 $m^2 g^{-1}$) combined with their highly tuneable framework architecture and chemical composition,[7] MOFs are emerging as an attractive platform for nanofluidic energy absorption. Hitherto, among the huge family of MOFs,[8] a few materials have been identified for this application,[9-13] mainly hydrothermally stable zeolitic imidazolate frameworks (ZIFs) consisting of hydrophobic nanocages.[14-16] However, current research has focused only on their performance under quasi-static loading conditions, *i.e.*, through slow intrusion and extrusion processes with typical strain rates of 10^{-5}-10^{-3} s^{-1}.[4,17] Some studies have started to investigate the influence of loading speed,[10,18,19] but remain far from realistic strain rates, which can exceed 10^3 s^{-1} for impact-attenuating materials.

Herein, we systematically investigate the response of various promising impact-attenuating MOFs, namely ZIF-8, ZIF-7, ZIF-9, ZIF-67, and ZIF-71, under practically relevant strain rates of up to 10^3 s^{-1}. Hereto, dynamic water intrusion-extrusion experiments using the dedicated high-rate experimental platform depicted in Fig. 1a-c were conducted. Most interestingly, the energy absorption densities of the investigated ZIF materials improve substantially upon increasing strain rate. Molecular dynamics (MD) simulations demonstrate that this beneficial effect originates from the intrinsic nanosecond timescale necessary for

water molecules to cluster in the ZIFs' hydrophobic nanocages and to facilitate transport across nanocages. This fundamental timescale, which increases the water intrusion pressure and energy absorption density at higher strain rates, depends on the cage-type geometry of the framework materials and is absent in channel-containing zeolites (ZSM-5, zeolite-β, mordenite). Based on these findings, four rules are formulated to design efficient and reusable energy-absorbing materials for high-rate mechanical impacts *via* the pressurized liquid intrusion mechanism, identifying ZIFs as a unique class of energy-absorbing materials. These generally applicable design rules are significant to further the development of nanofluidics, which has become a flourishing field over the last decade.[20]

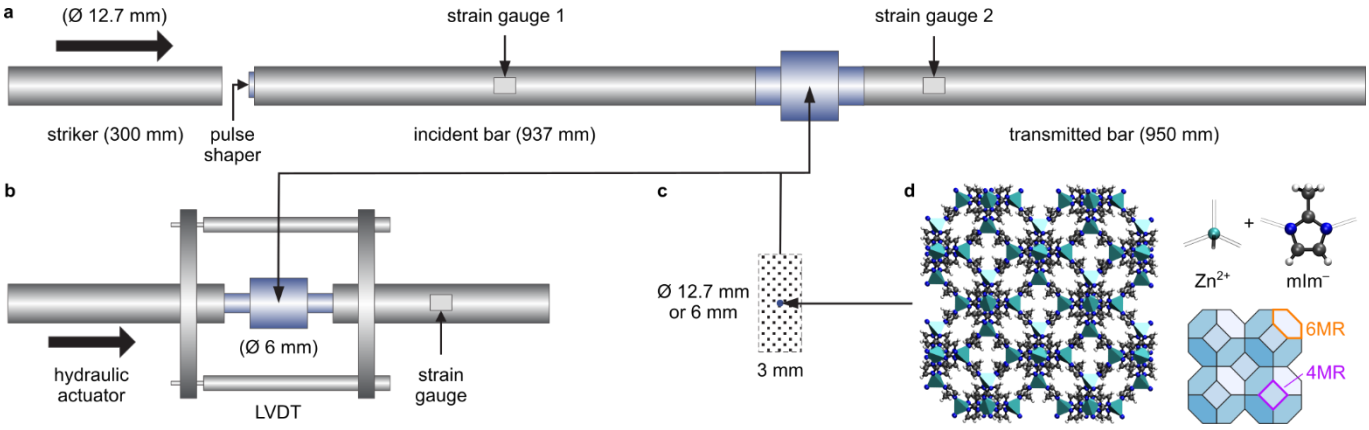

Fig. 1 | **Experimental Setup**. **a**, Split-Hopkinson-Pressure-Bar (SHPB) setup for high-rate experiments (10^3 s^{-1}). **b**, Hydraulic compression setup for medium-rate experiments (1-10^2 s^{-1}), with a pair of linear variable differential transformers (LVDTs) for displacement measurement. **c**, Water suspension of ZIF-8, which is sealed in stainless-steel chambers each with a pair of pistons (shown in **a**-**b**). **d**, Nanoporous framework structure, building blocks, and sodalite topology of ZIF-8 with indication of the 4-membered ring (4MR) and 6-membered ring (6MR) apertures. Low-rate experiments (up to 0.1 s^{-1}) are performed on a commercial screw driven testing machine (Instron 5582) using the stainless-steel chamber shown in **b**.

ZIF-8: Proof-of-concept for the strain rate dependent water intrusion and extrusion

We started our investigation with ZIF-8,[21] which is arguably the best-known ZIF for liquid intrusion studies.[9,17,18,22,23] ZIF-8 adopts the sodalite (**sod**) topology with relatively narrow apertures comprising 6-membered rings (6MR, aperture size ~3.40 Å) connecting larger internal cages (~11.6 Å, see Fig. 1d and Supplementary Section S1).[15] These two geometrical parameters correspond with the pore-limiting diameter (PLD) and the largest cavity diameter (LCD), respectively.

Fig. 2b shows the water intrusion and extrusion of ZIF-8 at different strain rates, $\dot{\varepsilon}$, encompassing six orders of magnitude from 10^{-3} s^{-1} to 10^{3} s^{-1}. As schematically indicated in Fig. 2a, three stages can be identified during loading. Initially and up to a strain, ε, of about 0.05 (equivalent to a specific volume change ΔV of ~0.17 cm^3 g^{-1}), the pressure increases linearly with the reduction in system volume. This is attributed to the elastic compression of the {ZIF-8+water} system, without any pore intrusion owing to ZIF-8's hydrophobicity. Next, the intrusion of water in the ZIF-8 nanocages gives rise to a plateau at the intrusion pressure P_{in}, until water molecules occupy the entire accessible pore volume. Afterwards, a linear reduction in system volume with increasing pressure is again observed. Similarly, the unloading curve shows an extrusion plateau, albeit at a lower extrusion pressure, P_{ex}, than the intrusion pressure, during which water escapes from the ZIF-8 cages.

As shown in Fig. 2c, the strain rate strongly affects the intrusion pressure, which almost triples from 25 MPa during the quasi-static compression to 70 MPa during the high-rate experiment. In contrast, the extrusion pressure experiences a drop with increasing strain rate. This yet-unidentified behaviour substantially increases the hysteresis and hence absorption capacity at the high loading rate compared to the quasi-static behaviour, eventually absorbing 85% of the mechanical energy stored during the intrusion process compared to only 17% at quasi-static conditions. Consequently, the energy absorption density, E_{ab}, is enhanced 17-fold, from ~3 J g^{-1} under quasi-static compression to ~47 J g^{-1} under high-rate loading representative of impact events. In contrast to other size-dependent MOF phenomena,[24,25] this enhanced absorption density can be obtained with different crystal sizes (see Supplementary Section S2.9).

To use this promising {ZIF-8+water} system as a reusable shock absorber, the intruded water molecules should eventually extrude from the framework. Fig. 2d presents five consecutive high-rate experiments, which exhibit a consistent performance subject to multiple impact cycles. Since the applied mechanical pressure is not yet high enough to cause structural amorphization,[26] the molecular structure of ZIF-8 remains intact, as evidenced from the X-ray diffraction patterns (Supplementary Fig. 4). Fig. 2e demonstrates that even when considering 1,000 loading-unloading cycles (at a strain rate of 0.03 s^{-1}), the performance reveals only a slight initial drop in the intrusion and extrusion pressure upon recycling. Furthermore, Fig. 2e shows that the system can be fully recovered after a 24 h relaxation (*i.e.*, with mechanical pressure removed), implying that all water molecules extrude from ZIF-8 given sufficient relaxation time. To further confirm the material stability and reusability, Supplementary Section S2.7 demonstrates that ZIF-8 is stable after twenty high-rate intrusion/extrusion cycles or after being immersed in water for over a week.

While the water intrusion rate during these experiments as well as its extrusion rate in the low-rate and medium-rate experiments are externally controlled through the displacement rate, the high-rate SHPB setup of Fig. 1a leads to a free water extrusion process which represents the performance under realistic impact and reveals the intrinsic timescale of water mobility in ZIF-8. Fig. 2c reveals that this intrinsic water extrusion occurs at a much lower rate than its externally driven intrusion process (10^2 s^{-1} *vs.* 10^3 s^{-1}, see also Supplementary Fig. 12), corroborating the earlier observation that some water molecules remain in the structure when the system is not allowed to relax sufficiently between different cycles. High-rate experiments with different loading pulses indicate that water extrusion starts at a higher rate, which then gradually decreases, indicating a higher water mobility when more water is present inside the framework (see Supplementary Fig. 13).

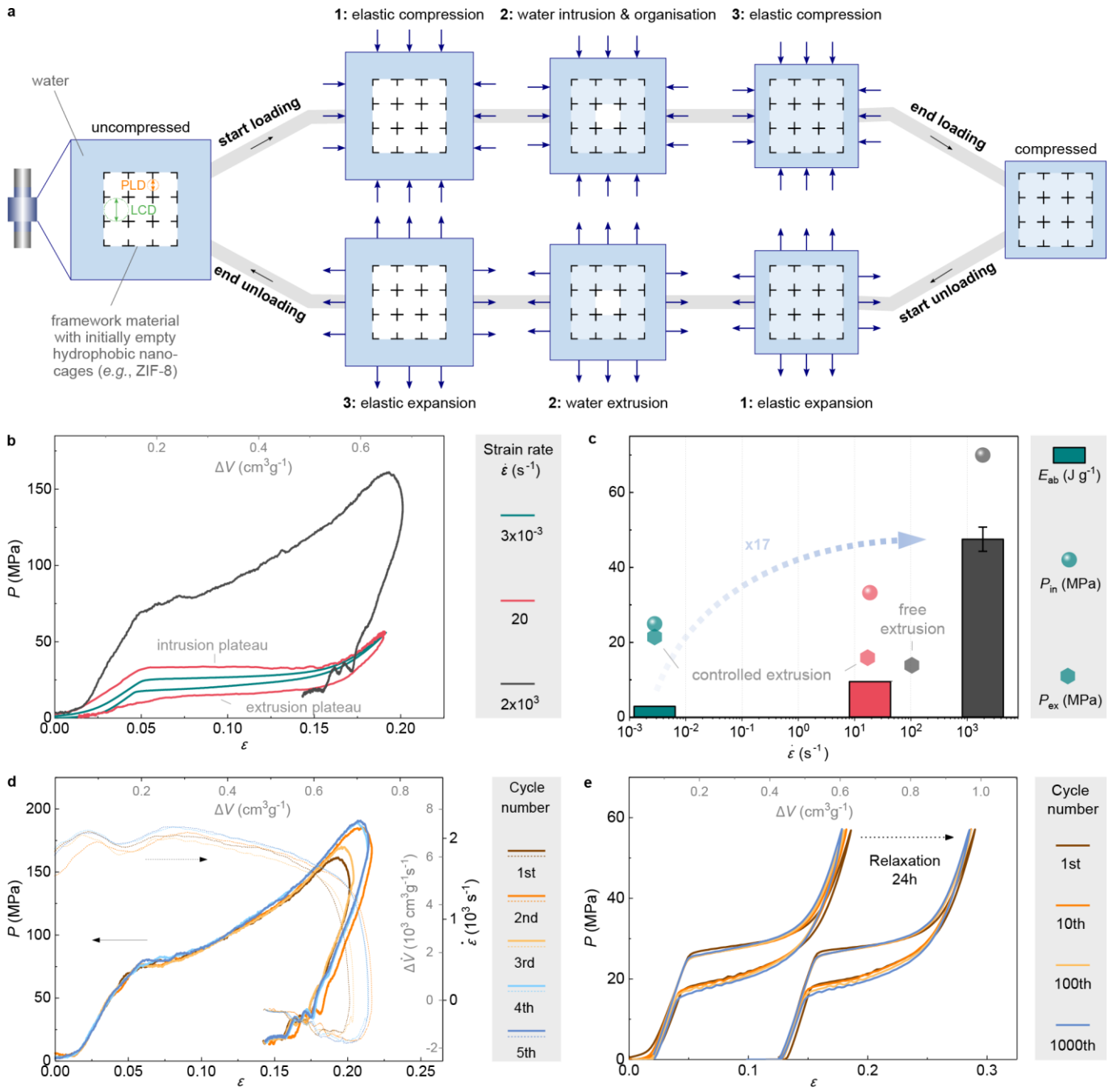

Fig. 2 | Water intrusion and extrusion of ZIF-8 at low-rate, medium-rate, and high-rate loading conditions. a, Schematic overview of the different processes during compression (top) and expansion (bottom), including the water intrusion/extrusion processes that give rise to distinct plateaus and indication of the PLD and LCD of the nanoporous material. **b**, Compressive stress-strain curves at three different strain rates corresponding to a specific volume change rate $\Delta\dot{V}$ of 1×10^{-2}, 70, and 7×10^{3} $cm^3\,g^{-1}\,s^{-1}$, respectively. The unloading part of the high-rate experiment is uncontrolled (*i.e.*, without external driving force), so only part of the extrusion plateau can be recorded. **c**, Intrusion pressure, extrusion pressure, and energy absorption density under three different loading conditions, plotted as a function of the intrusion and extrusion strain rates measured by the SHPB technique (see also Supplementary Fig. 12). The error bar represents the uncertainty due to the incomplete unloading curve at high strain rate. **d**, Five consecutive

high-rate experiments (~6 min interval between each cycle), showing consistent performance against multiple impacts. The small variation in their responses can be attributed to the strain rate history shown as the dashed lines in the graph. **e**, 1,000 intrusion-extrusion cycles at a strain rate of 0.03 s^{-1} (or 0.1 cm^3 g^{-1} s^{-1}), confirming the durability of the system. After 24 h relaxation during which the sample was kept under no mechanical pressure, another set of 1,000 cycles was recorded. The intrusion-extrusion cycles after relaxation are horizontally offset by a value of 0.12 for clarity.

The intrinsic water mobility timescale revealed by molecular dynamics simulations

These experiments unveil a highly interesting mechanism, in which the ZIF-8 energy absorption capacity critically increases with increasing strain rate. While this is expected to be related to the mobility and reorganisation of water in the nanocages, it is necessary to understand the nanoscale origin of this phenomenon to fully explore the potential of the rate-dependent intrusion-extrusion performance and generalise it towards other materials. To this end, MD simulations were conducted using a fully flexible and *ab initio* derived ZIF-8 force field. This force field is validated in Supplementary Section S3 and complemented by the flexible TIP4P/2005f water model,[27] given its agreement with experimental adsorption isotherms.[16,28,29]

First, grand canonical Monte Carlo simulations were performed, revealing that water saturation in ZIF-8 is obtained at ~80 molecules per unit cell (see Supplementary Section S4.1) or, equivalently, ~40 molecules per cage, in excellent agreement with previous studies.[16,28,29] Subsequently, snapshots at different water loadings were extracted to start separate canonical Monte Carlo simulations. Fig. 3a reveals the distribution of these water molecules in ZIF-8 for the different cross-sections defined in Fig. 3b. At low water loading, distinct crystallographic adsorption sites are detected, which can be compared to the experimental argon adsorption sites by Hobday *et al.*[30] For water, the most favourable adsorption sites are located between the 4MR and 6MR apertures (site Ar-2 in Ref. 30) and near the 4MR apertures (site Ar-4 in Ref. 30). Notably, no water is adsorbed directly inside either the 4MR or 6MR apertures, although the 6MR apertures are the most favourable adsorption sites for argon.[30] At high water loadings, the water molecules agglomerate around the cage centre due to ZIF-8's hydrophobicity, partaking in a hydrogen-bonded cluster that provides more favourable interactions than the ZIF-8 framework.

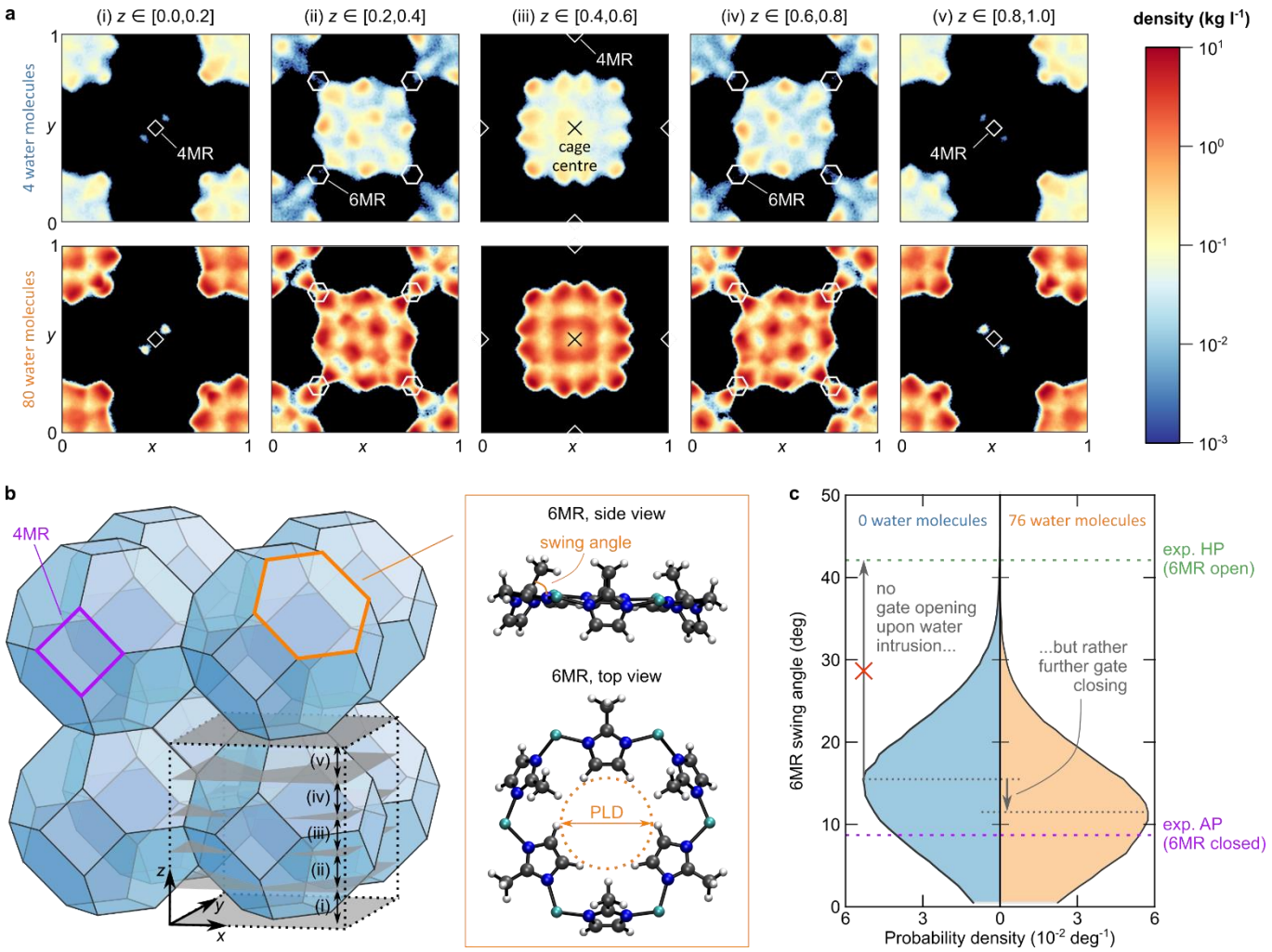

Fig. 3 | Simulated water distribution in ZIF-8 and its effect on gate opening. a, Symmetrised water density from a 2×2×2 ZIF-8 simulation cell as obtained from canonical Monte Carlo simulations at 298 K with either 4 or 80 water molecules per unit cell in the ambient pressure (AP) phase. The axes are defined in fractional coordinates and the unit cell is sliced in five equal slabs for clarity (see **b**). The 4MR and 6MR apertures connecting the cages are denoted by (truncated) diamonds and hexagons, respectively. Other water loadings are shown in Supplementary Section S4.2. **b,** The ZIF-8 topology with the cross-sections used for the density plots in **a** as well as the 4MR and 6MR apertures. Atomistic representation of the 6MR aperture, showing in orange the pore limiting diameter (PLD) and 6MR swing angle. **c,** Probability density of the 6MR dihedral swing angle of ZIF-8 during a 5 ns MD simulation at 300 K and 0 MPa with either 0 or 76 water molecules per ZIF-8 unit cell. Experimental AP and HP (high pressure) phases are indicated in purple and green, respectively.[31] Swing angle distributions and X-ray diffraction patterns at other water loadings and increased mechanical pressures are shown in Supplementary Section S5, while the swing angle distributions obtained through *ab initio* MD simulations at various temperatures are shown in Supplementary Section S6.

Subsequently, 300 K MD simulations of fully flexible ZIF-8 structures were performed, confirming that water avoids the 6MR apertures, irrespective of the applied pressure (see Supplementary Section S7). As a result, without a driving force, water molecules seldom hop between ZIF-8 cages. However, an increasing water loading facilitates hopping and hence enables water transport (see Supplementary Section S7.2). This agrees well with the higher water mobility at the onset of the extrusion experiments, when more water is present in the cages (see Supplementary Section S2.2). To understand whether this water mobility can be attributed to structural effects such as gate opening, the swing angle defining the 6MR aperture and the associated PLD (see Fig. 3b) are monitored.[32] As shown in Fig. 3c and Ref. 23, higher water loadings do not lead to the anticipated gate opening but rather close the 6MR aperture even further.

To mimic water mobility more closely, an inhomogeneous water distribution inside a 1×1×2 supercell of ZIF-8 was created, which only contains 42 water molecules in cage 1, as shown in Fig. 4a. During the MD simulation, this water gradient steers the molecules from cage 1 towards the neighbouring cages 2 and 3 through the 6MR apertures, despite their hydrophobicity (see Fig. 4b). After 0.45 ns, six and two water molecules have diffused to cages 2 and 3, respectively (see Fig. 4c(ii)). While the six water molecules in cage 2 form a stable hydrogen-bonded cluster, the two in cage 3 are insufficiently stabilised and diffuse back into cage 1 – against the water gradient. The water cluster inside cage 2 continues to grow as the existing cluster facilitates further hopping from cage 1 to 2. An exponential fit to the number of water molecules in cage 2 reveals that this nucleation process occurs on a nanosecond timescale (see Fig. 4b), independent of the cages in which the cluster nucleates and the ZIF-8 model size (Supplementary Section S8).

To further quantify the free energy barrier of the nucleation process, the umbrella sampling (US) free energy profiles associated with a water molecule transitioning from cage 1 to 2 are shown in Fig. 4d and Supplementary Section S9.3. Herein, besides the water molecule that undergoes the transition, cage 1 contained a critical-sized cluster of five water molecules while cage 2 contained in between zero and five water molecules. Fig. 4d and Supplementary Table 3 indicate that, while the empty cage 2 (CV > 0 Å) is substantially less favourable than cage 1 (CV < 0 Å), with free energy differences ΔF up to 15 kJ mol^{-1}, the

transition of additional water molecules is facilitated once a critical-sized cluster of about four water molecules is present in cage 2. Fig. 4d therefore confirms that the slow nucleation of such critical-sized water clusters is crucial to facilitate water diffusion through ZIF-8's hydrophobic cages, in agreement with Fig. 4b.

This observation also explains the substantial increase in intrusion pressure and energy absorption density at higher strain rates in Fig. 2c. Since the intrinsic intrusion process is hypothesised to occur through the nucleation of critical-sized water clusters, the timescale for nucleation can be associated with an intrinsic strain rate (see Supplementary Section S8.3). If the externally applied strain rate is lower than this intrinsic rate, critical-sized water clusters will spontaneously nucleate in cages neighbouring already filled cages, facilitating the further intrusion process. However, if the strain rate exceeds this intrinsic rate, critical-sized water clusters cannot organise in time and additional work needs to be exerted – through an increased input pressure – to help overcome the free energy barrier of the 6MR aperture. This also implies that water molecules remaining in the ZIF-8 cages during the extrusion process due to insufficient relaxation will facilitate the subsequent intrusion process and lower the intrusion pressure, as confirmed by Fig. 2e.

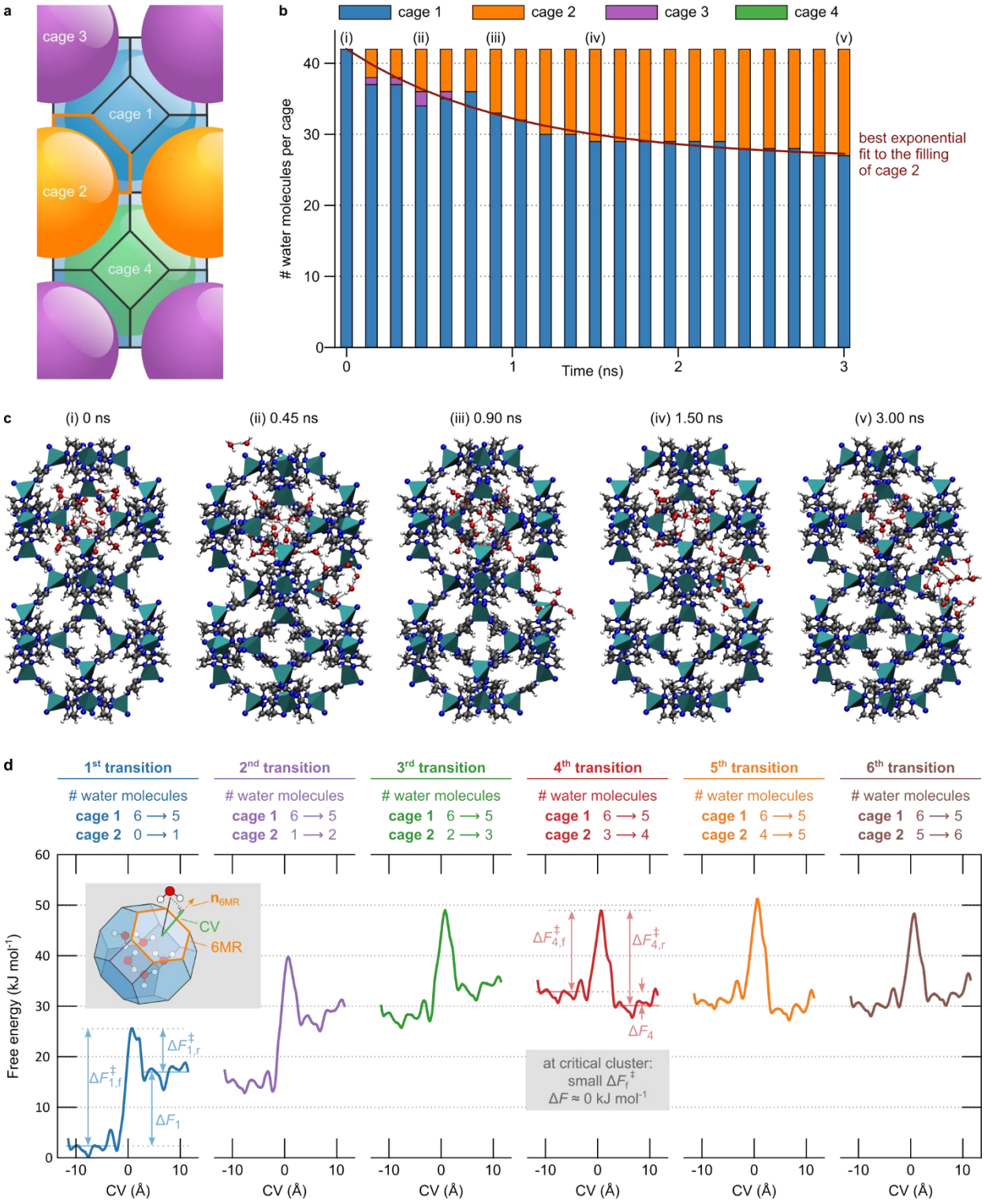

Fig. 4 | Determining the intrinsic timescale for water mobility in the ZIF-8 nanocages by non-equilibrium MD simulations. a, A 1×1×2 ZIF-8 supercell with four inequivalent cages connected through 6MR apertures. **b,** Evolution of the number of water molecules per cage at 300 K and 0 MPa when starting from 42 water molecules in cage 1 while all other cages are initially empty. The best exponential fit of $a\left(1-\mathrm{e}^{-t/\tau}\right)$ to the filling of cage 2 (red line) yields a time constant $\tau \sim 1$ ns (see statistical analysis in Supplementary Section S8). **c,** Visualization of water-filled ZIF-8 structures at five representative points during the simulation; a full water cluster analysis is provided in

Supplementary Section S9.4. **d,** Free energy profiles associated with a water molecule transitioning from cage 1, containing a critical-sized water cluster of five additional molecules, to cage 2, initially containing in between zero (first transition) and five (sixth transition) water molecules. Results obtained through six independent sets of umbrella sampling (US) simulations using a similar collective variable (CV, see figure inset) as in Ref. 33. Additional US simulations are reported in Supplementary Section S9.3.

Generalisation of the rate effect and design rules

The here established water intrusion mechanism for ZIF-8 suggests that other materials that are constructed from nanocages connected through hydrophobic narrow apertures could also exhibit the rate-dependent water intrusion behaviour. To derive generally applicable design rules, we repeated the water intrusion experiments on a group of hydrophobic ZIFs, namely ZIF-67, ZIF-7, ZIF-9, and ZIF-71 (see Supplementary Fig. 1), leading to the energy absorption densities and intrusion pressures shown in Fig. 5a and Supplementary Fig. 14.

Fig. 5b,d and Supplementary Fig. 16 demonstrate that ZIF-67 and ZIF-71 exhibit the attractive rate dependence and reusability, confirming the ZIF-8 as proof-of-concept. For ZIF-71, a very high intrusion pressure, exceeding 150 MPa, under a loading rate of ~2,000 s^{-1} is expected (see Supplementary Fig. 15). However, for ZIF-7 and ZIF-9, water is permanently trapped inside (Fig. 5c). This is probably due to their smaller PLDs, as their hydrophobic apertures are narrower than the size of water molecules.[12] Therefore, ZIF-7 and ZIF-9 can only be reused after evacuating the intruded water molecules by heat treatment to regain the original porosity,[12] in contrast to ZIF-8, ZIF-67, and ZIF-71, which can be directly reused to absorb multiple impacts. Finally, the comparison between the structural analogues, ZIF-8 *vs.* ZIF-67 (Fig. 5d), and ZIF-7 *vs.* ZIF-9 (Fig. 5c), suggests that the influence of the chemical moieties is very limited.

Based on these experimental observations, four general rules emerge that can be used to design mechanical impact absorbers leveraging the high-rate water intrusion mechanism:

1. The material should be hydrophobic;
2. The material should consist of nanocages, *i.e.*, LCD > PLD;
3. The apertures connecting the nanocages should be sufficiently large to ensure reusability. Based on our experimental observations on ZIF-11 and ZIF-12 (see Supplementary Fig. 17), the PLD threshold value is ~3 Å for water intrusion systems;
4. Larger nanocages can accommodate larger water clusters and hence increase the energy absorption density at high strain rates.

In Fig. 5e and Supplementary Section S10, the 105 ZIF-like materials tabulated in Ref. 34 are tested against these design rules. Fig. 5e demonstrates that, besides the here validated ZIF-8, ZIF-67, and ZIF-71, our design rules identify an additional 17 materials as potential high-performance impact-attenuating materials *via* the high-rate water intrusion mechanism depicted in Fig. 2a. These design rules can furthermore be generalised to other porous zeolite frameworks, as validated for chabazite in Supplementary Section S2.8.

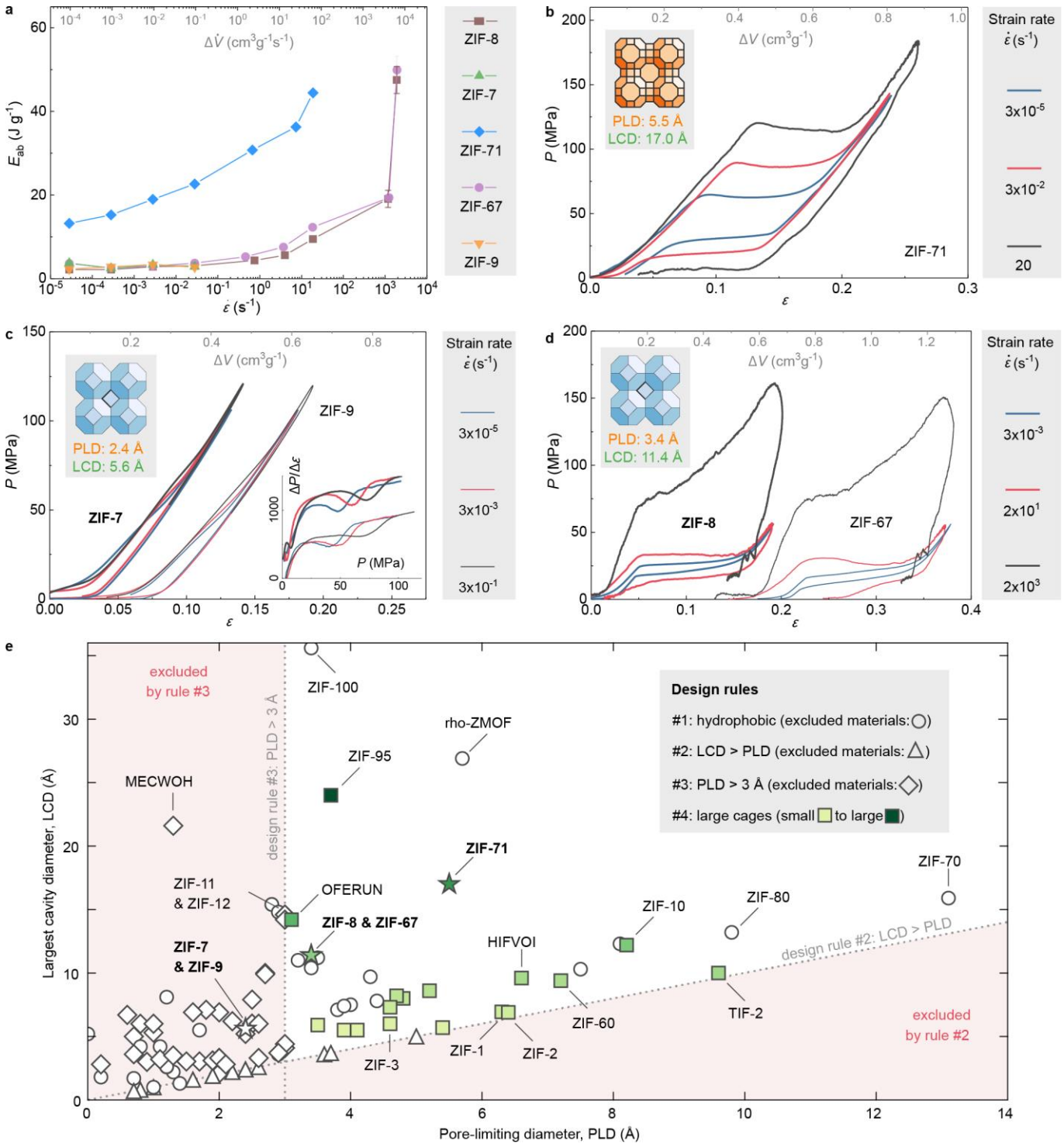

Fig. 5 | Generalisation of the design rules. a, Energy absorption densities of various hydrophobic cage-type ZIFs as a function of the strain rate. The error bars represent the uncertainty due to the incomplete unloading curves. **b**, Water intrusion and extrusion of ZIF-71 at three different strain rates, which correspond to a specific volume change rate $\Delta\dot{V}$ of 1×10^{-4}, 1×10^{-1}, and 80 $cm^3\,g^{-1}\,s^{-1}$, respectively. **c**, Water intrusion of ZIF-7 and ZIF-9 at three different strain rates, which correspond to $\Delta\dot{V}$ of 1×10^{-4}, 1×10^{-2}, and 1 $cm^3\,g^{-1}\,s^{-1}$, respectively. Their intrusion pressures, which can be identified from the $\Delta P/\Delta\varepsilon$ during loading process (inset), increase with the strain rate as design rule #2 is satisfied, although design rule #3 is violated. **d**, Water intrusion and extrusion of ZIF-8 and ZIF-67 at three different

strain rates, which correspond to $\Delta\dot{V}$ of 1×10^{-2}, 70, and 7×10^{3} $cm^3\,g^{-1}\,s^{-1}$, respectively. Plots in **c** and **d** are offset horizontally for clarity. **e**, Materials selection map of the 105 ZIFs tabulated in Ref. 34 and Supplementary Section S10 according to their PLD and LCD, showing 20 promising materials fulfilling our design rules (□ to ■); others are either not hydrophobic (as determined by their linkers, ○), not cage-type (△), or have too small a PLD (◇). Experimentally validated materials are bold-faced (☆).

Contrasting against channel-containing frameworks

To further test our hypothesis that the cage-type structure is essential for the rate-dependent intrusion-extrusion phenomenon of ZIFs (design rule #2), we performed water intrusion experiments for several typical channel-containing zeolites, namely ZSM-5, zeolite-β, and mordenite (see Supplementary Fig. 2). Supporting our hypothesis, Fig. 6a reveals that the rate dependence of their intrusion pressure is considerably weaker than for ZIFs. The same is true for their extrusion pressure, which is always located near the magnitude of the intrusion pressure, leading to a hysteresis area and energy absorption density that are not substantially enhanced by high loading rates (see Fig. 6d and Supplementary Section S11).

Explicitly contrasting ZSM-5 and ZIF-8 in Fig. 6c-d reveals a much higher spontaneous extrusion rate in the former. Furthermore, ZIF-8 exhibits a slight increase of the gradient with the intrusion rate (Fig. 2b), which is absent for ZSM-5 (Fig. 6b). Both observations suggest that the water flow inside channel-containing structures experiences a much lower transport resistance, in agreement with previous reports observing enhanced flow in small channels.[35-40] This suggests the advantage under high-rate mechanical impact of cage-type structures, which can be made into efficient and reusable energy absorbers thanks to the intrinsic nanosecond time scale for water organisation, over more frequently used channel-containing structures, which perform as non-linear springs with an insignificant rate dependence.

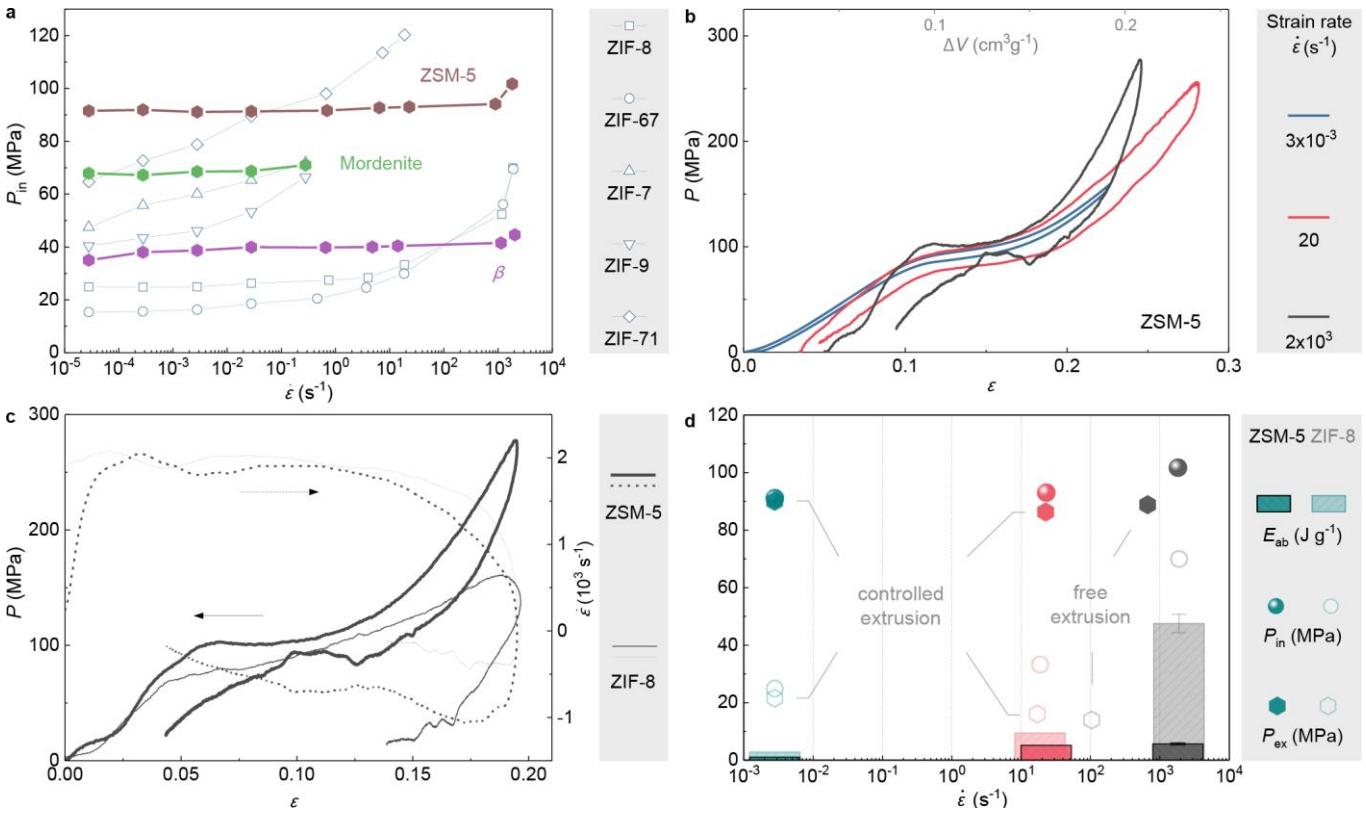

Fig. 6 | Water intrusion and extrusion of channel-containing zeolites at different conditions. a, Water intrusion pressure as a function of strain rate, comparing the behaviour of channel-containing zeolites against cage-type ZIFs. Due to the limited pore volume of mordenite, its intrusion pressure at higher loading rate is not available. **b**, Water intrusion and extrusion of ZSM-5 at three different strain rates, which correspond to a specific volume change rate $\Delta\dot{V}$ of 2×10^{-3}, 20, and 2×10^{3} $cm^3\,g^{-1}\,s^{-1}$, respectively. **c**, Comparison between ZIF-8 and ZSM-5 under high-rate deformation. **d,** Intrusion pressure, extrusion pressure, and energy absorption density of ZSM-5 (dark colour and filled symbols) at the three different conditions, compared with ZIF-8 (light colour and open symbols). The error bars represent the uncertainty due to the incomplete unloading curves at high strain rates.

Discussion

Developing efficient impact-attenuating materials is an important societal challenge for a wide variety of applications, with current state-of-the-art energy absorption materials often showing a poor efficiency or recoverability in cyclic loading. Herein, we discovered a promising approach to mitigate mechanical impact under industrially relevant impact conditions and associated high strain rates. We revealed that the energy absorption density associated with the forced intrusion of liquid water in framework materials containing nanocages separated by hydrophobic apertures critically depends on the strain rate. Based on this concept, {ZIF+water} systems are remarkably effective as high-rate nanofluidic energy absorbers for mitigating mechanical impacts at realistic strain rates of 10^3 s^{-1}.

The ZIF-8 material serves as a proof-of-concept, for which we observed a sharp rise in energy absorption density with elevating strain rates, stemming from the major enhancement of the hysteresis bound by the water intrusion-extrusion curves. Surprisingly, the fundamental process underpinning this rate-dependent water intrusion did not depend on the gate-opening mechanism that dominates its gas adsorption behaviour. Instead, we established that the unique rate-dependence is controlled by the intrinsic timescale to form critically-sized and stable hydrogen-bonded clusters in the hydrophobic cages, as they facilitate the inefficient water transport through the hydrophobic apertures separating adjacent cages. Because externally controlling the water intrusion beyond this intrinsic timescale requires substantially higher intrusion pressures, we observed a significant rise in energy absorption density at higher strain rates. We showed that this ZIF-8 proof-of-concept can be generalized to several other cage-type ZIFs, whereas it is absent for channel-containing zeolites. Based on these theoretical and experimental observations, four design rules were formulated to construct high-rate energy absorption materials, thereby identifying 17 more potential candidate materials. These generally applicable design rules shed light on the synergistic role played by the framework architecture and hydrophobicity during forced water intrusion, which are key to the design and tuning of nanoporous materials such as ZIFs towards practical and reusable impact-attenuating materials.

References

1. Lu, G. & Yu, T. *Energy Absorption of Structures and Materials*. (Woodhead Publishing Limited, Cambridge, 2003).
2. Gibson, L. J. & Ashby, M. F. *Cellular Solids: Structure and Properties*. 2nd edn, (Cambridge University Press, Cambridge, 1997).
3. Clough, E. C. *et al.* Elastomeric microlattice impact attenuators. *Matter* **1**, 1519-1531 (2019).
4. Fraux, G., Coudert, F. X., Boutin, A. & Fuchs, A. H. Forced intrusion of water and aqueous solutions in microporous materials: from fundamental thermodynamics to energy storage devices. *Chem. Soc. Rev.* **46**, 7421-7437 (2017).
5. Eroshenko, V., Regis, R.-C., Soulard, M. & Patarin, J. Energetics: A new field of applications for hydrophobic zeolites. *J. Am. Chem. Soc.* **123**, 8129-8130 (2001).
6. Tinti, A., Giacomello, A., Grosu, Y. & Casciola, C. M. Intrusion and extrusion of water in hydrophobic nanopores. *Proc. Natl. Acad. Sci. USA* **114**, E10266-E10273 (2017).
7. Furukawa, H., Cordova, K. E., O'Keeffe, M. & Yaghi, O. M. The chemistry and applications of metal-organic frameworks. *Science* **341**, 1230444 (2013).
8. Moghadam, P. Z. *et al.* Development of a Cambridge Structural Database subset: a collection of metal–organic frameworks for past, present, and future. *Chem. Mater.* **29**, 2618-2625 (2017).
9. Ortiz, G., Nouali, H., Marichal, C., Chaplais, G. & Patarin, J. Energetic performances of the metal–organic framework ZIF-8 obtained using high pressure water intrusion–extrusion experiments. *Phys. Chem. Chem. Phys.* **15**, 4888-4891 (2013).
10. Grosu, Y. *et al.* Stability of zeolitic imidazolate frameworks: effect of forced water intrusion and framework flexibility dynamics. *RSC Adv.* **5**, 89498-89502 (2015).
11. Ortiz, G., Nouali, H., Marichal, C., Chaplais, G. & Patarin, J. l. Energetic performances of "ZIF-71-aqueous solution" systems: A perfect shock-absorber with water. *J. Phys. Chem. C* **118**, 21316-21322 (2014).
12. Sun, Y., Li, Y. & Tan, J. C. Liquid intrusion into zeolitic imidazolate framework-7 nanocrystals: Exposing the roles of phase transition and gate opening to enable energy absorption applications. *ACS Appl. Mater. Interfaces* **10**, 41831-41838 (2018).
13. Grosu, Y. *et al.* A highly stable nonhysteretic {Cu2 (tebpz) MOF+water} molecular spring. *ChemPhysChem* **17**, 3359-3364 (2016).

14. Park, K. S. *et al.* Exceptional chemical and thermal stability of zeolitic imidazolate frameworks. *Proc. Natl. Acad. Sci. USA* **103**, 10186 (2006).

15. Banerjee, R. *et al.* High-throughput synthesis of zeolitic imidazolate frameworks and application to CO_2 capture. *Science* **319**, 939 (2008).

16. Ortiz, A. U., Freitas, A. P., Boutin, A., Fuchs, A. H. & Coudert, F.-X. What makes zeolitic imidazolate frameworks hydrophobic or hydrophilic? The impact of geometry and functionalization on water adsorption. *Phys. Chem. Chem. Phys.* **16**, 9940-9949 (2014).

17. Khay, I. *et al.* Assessment of the energetic performances of various ZIFs with SOD or RHO topology using high pressure water intrusion-extrusion experiments. *Dalton Trans.* **45**, 4392-4400 (2016).

18. Sun, Y., Li, Y. & Tan, J. C. Framework flexibility of ZIF-8 under liquid intrusion: discovering time-dependent mechanical response and structural relaxation. *Phys. Chem. Chem. Phys.* **20**, 10108-10113 (2018).

19. Lowe, A. *et al.* Effect of flexibility and nanotriboelectrification on the dynamic reversibility of water intrusion into nanopores: Pressure-transmitting fluid with frequency-dependent dissipation capability. *ACS Appl. Mater. Interfaces* **11**, 40842-40849 (2019).

20. Bocquet, L. Nanofluidics coming of age. *Nat. Mater.* **19**, 254-256 (2020).

21. Huang, X. C., Lin, Y. Y., Zhang, J. P. & Chen, X. M. Ligand-directed strategy for zeolite-type metal-organic frameworks: zinc(II) imidazolates with unusual zeolitic topologies. *Angew. Chem. Int. Ed.* **45**, 1557-1559 (2006).

22. Khay, I., Chaplais, G., Nouali, H., Marichal, C. & Patarin, J. Water intrusion–extrusion experiments in ZIF-8: impacts of the shape and particle size on the energetic performances. *RSC Adv.* **5**, 31514-31518 (2015).

23. Fraux, G., Boutin, A., Fuchs, A. H. & Coudert, F.-X. Structure, dynamics, and thermodynamics of intruded electrolytes in ZIF-8. *J. Phys. Chem. C* **123**, 15589-15598 (2019).

24. Sakata, Y. *et al.* Shape-memory nanopores induced in coordination frameworks by crystal downsizing. *Science* **339**, 193-196 (2013).

25. Krause, S. *et al.* The effect of crystallite size on pressure amplification in switchable porous solids. *Nat. Commun.* **9**, 1-8 (2018).

26. Bennett, T. D. & Cheetham, A. K. Amorphous metal-organic frameworks. *Acc. Chem. Res.* **47**, 1555-1562 (2014).

27. Gonzalez, M. A. & Abascal, J. L. A flexible model for water based on TIP4P/2005. *J. Chem. Phys.* **135**, 224516 (2011).

28. Ghosh, P., Kim, K. C. & Snurr, R. Q. Modeling water and ammonia adsorption in hydrophobic metal-organic frameworks: Single components and mixtures. *J. Phys. Chem. C* **118**, 1102-1110 (2014).

29. Zhang, H. & Snurr, R. Q. Computational study of water adsorption in the hydrophobic metal-organic framework ZIF-8: Adsorption mechanism and acceleration of the simulations. *J. Phys. Chem. C* **121**, 24000-24010 (2017).

30. Hobday, C. L. *et al.* Understanding the adsorption process in ZIF-8 using high pressure crystallography and computational modelling. *Nat. Commun.* **9**, 1429 (2018).

31. Moggach, S. A., Bennett, T. D. & Cheetham, A. K. The effect of pressure on ZIF-8: increasing pore size with pressure and the formation of a high-pressure phase at 1.47 GPa. *Angew. Chem. Int. Ed.* **48**, 7087-7089 (2009).

32. Durholt, J. P., Fraux, G., Coudert, F. X. & Schmid, R. Ab initio derived force fields for zeolitic imidazolate frameworks: MOF-FF for ZIFs. *J. Chem. Theory Comput.* **15**, 2420-2432 (2019).

33. Cnudde, P. *et al.* Light Olefin Diffusion during the MTO Process on H-SAPO-34: A Complex Interplay of Molecular Factors. *J. Am. Chem. Soc.* **142**, 6007-6017 (2020).

34. Phan, A. *et al.* Synthesis, structure, and carbon dioxide capture properties of zeolitic imidazolate frameworks. *Acc. Chem. Res.* **43**, 58-67 (2010).

35. Majumder, M., Chopra, N., Andrews, R. & Hinds, B. J. Enhanced flow in carbon nanotubes. *Nature* **438**, 44-44 (2005).

36. Holt, J. K. *et al.* Fast mass transport through sub-2-nanometer carbon nanotubes. *Science* **312**, 1034-1037 (2006).

37. Secchi, E. *et al.* Massive radius-dependent flow slippage in carbon nanotubes. *Nature* **537**, 210-213 (2016).

38. Radha, B. *et al.* Molecular transport through capillaries made with atomic-scale precision. *Nature* **538**, 222-225 (2016).

39. Tunuguntla, R. H. *et al.* Enhanced water permeability and tunable ion selectivity in subnanometer carbon nanotube porins. *Science* **357**, 792-796 (2017).

40. Keerthi, A. *et al.* Ballistic molecular transport through two-dimensional channels. *Nature* **558**, 420-424 (2018).

Correspondence and requests for materials should be addressed to Y.S., S.M.J.R., V.V.S, or J.-C.T.

Acknowledgments

Y.S. and J.-C.T. wish to thank the K.C. Wong Fellowship (Y.S.) and the ERC Consolidator Grant (under the grant agreement 771575 PROMOFS (J.-C.T.)) for funding the research. Y.S. also wishes to thank the University of Birmingham for startup funds. S.M.J.R., A.L, S.V.D.B., and J.W wish to thank the Fund for Scientific Research Flanders (FWO, grant nos. 12T3519N (S.M.J.R.), 11D2220N (A.L.), 11U1914N (S.V.D.B), and 1103618N (J.W.)) and the Research Board of Ghent University (BOF). Funding was also received from the European Union's Horizon 2020 Research and Innovation Programme [ERC Consolidator Grant Agreement 647755 – DYNPOR (2015-2020) (V.V.S.)]. We thank the Research Complex at Harwell (RCaH) for access to the materials characterization facilities, and Dr. Timothy Johnson at Johnson Matthey Technology Centre for providing the chabazite material. The computational resources (Stevin Supercomputer Infrastructure) and services used in this work were provided by the VSC (Flemish Supercomputer Centre), funded by Ghent University, the Research Foundation – Flanders (FWO), and the Flemish Government – department EWI.

Author contributions

Y.S. conceived and performed all experiments, with guidance from C.R.S. and J.-C.T. S.M.J.R. performed the force-field based MD simulations, A.L. performed the *ab initio* and umbrella sampling MD simulations, S.V. performed the GCMC and canonical MC simulations, and J.W. derived the ZIF-8 covalent force field, all under guidance of V.V.S. Y.S., S.M.J.R., J.-C.T., and V.V.S wrote the manuscript with contributions of all authors.

Competing interests

The authors declare no competing interests.

Figure legends (for main text figures)

Fig. 1 | Experimental Setup. **a**, Split-Hopkinson-Pressure-Bar (SHPB) setup for high-rate experiments (10^3 s^{-1}). **b**, Hydraulic compression setup for medium-rate experiments (1-10^2 s^{-1}), with a pair of linear variable differential transformers (LVDTs) for displacement measurement. **c**, Water suspension of ZIF-8, which is sealed in stainless-steel chambers each with a pair of pistons (shown in **a**-**b**). **d**, Nanoporous framework structure, building blocks, and sodalite topology of ZIF-8 with indication of the 4-membered ring (4MR) and 6-membered ring (6MR) apertures. Low-rate experiments (up to 0.1 s^{-1}) are performed on a commercial screw driven testing machine (Instron 5582) using the stainless-steel chamber shown in **b**.

Fig. 2 | Water intrusion and extrusion of ZIF-8 at low-rate, medium-rate, and high-rate loading conditions. a, Schematic overview of the different processes during compression (top) and expansion (bottom), including the water intrusion/extrusion processes that give rise to distinct plateaus and indication of the PLD and LCD of the nanoporous material. **b**, Compressive stress-strain curves at three different strain rates corresponding to a specific volume change rate $\Delta\dot{V}$ of 1×10^{-2}, 70, and 7×10^3 $cm^3\,g^{-1}\,s^{-1}$, respectively. The unloading part of the high-rate experiment is uncontrolled (*i.e.,* without external driving force), so only part of the extrusion plateau can be recorded. **c**, Intrusion pressure, extrusion pressure, and energy absorption density under three different loading conditions, plotted as a function of the intrusion and extrusion strain rates measured by the SHPB technique (see also Supplementary Fig. 12). The error bar represents the uncertainty due to the incomplete unloading curve at high strain rate. **d**, Five consecutive high-rate experiments (~6 min interval between each cycle), showing consistent performance against multiple impacts. The small variation in their responses can be attributed to the strain rate history shown as the dashed lines in the graph. **e**, 1,000 intrusion-extrusion cycles at a strain rate of 0.03 s^{-1} (or 0.1 $cm^3\,g^{-1}\,s^{-1}$), confirming the durability of the system. After 24 h relaxation during which the sample was kept under no mechanical pressure, another set of 1,000 cycles was recorded. The intrusion-extrusion cycles after relaxation are horizontally offset by a value of 0.12 for clarity.

Fig. 3 | Simulated water distribution in ZIF-8 and its effect on gate opening. a, Symmetrised water density from a 2×2×2 ZIF-8 simulation cell as obtained from canonical Monte Carlo simulations at 298 K with either 4 or 80 water molecules per unit cell in the ambient pressure (AP) phase. The axes are defined in fractional coordinates and the unit cell is sliced in five equal slabs for clarity (see **b**). The 4MR and 6MR apertures connecting the cages are denoted by (truncated) diamonds and hexagons, respectively. Other water loadings are shown in Supplementary Section S4.2. **b,** The ZIF-8 topology with the cross-sections used for the density plots in **a** as well as the 4MR and 6MR apertures. Atomistic representation of the 6MR aperture, showing in orange the pore limiting diameter (PLD) and 6MR swing angle. **c,** Probability density of the 6MR dihedral swing angle of ZIF-8 during a 5 ns MD simulation at 300 K and 0 MPa with either 0 or 76 water molecules per ZIF-8 unit cell. Experimental AP and HP (high pressure) phases are indicated in purple and green, respectively.[31] Swing angle distributions and X-ray diffraction patterns at other water loadings and increased mechanical pressures are shown in Supplementary Section S5, while the swing angle distributions obtained through *ab initio* MD simulations at various temperatures are shown in Supplementary Section S6.

Fig. 7 | Determining the intrinsic timescale for water mobility in the ZIF-8 nanocages by non-equilibrium MD simulations. a, A 1×1×2 ZIF-8 supercell with four inequivalent cages connected through 6MR apertures. **b,** Evolution of the number of water molecules per cage at 300 K and 0 MPa when starting from 42 water molecules in cage 1 while all other cages are initially empty. The best exponential fit of $a\left(1-\mathrm{e}^{-t/\tau}\right)$ to the filling of cage 2 (red line) yields a time constant $\tau\sim1$ ns (see statistical analysis in Supplementary Section S8). **c,** Visualization of water-filled ZIF-8 structures at five representative points during the simulation; a full water cluster analysis is provided in Supplementary Section S9.4. **d,** Free energy profiles associated with a water molecule transitioning from cage 1, containing a critical-sized water cluster of five additional molecules, to cage 2, initially containing in between zero (first transition) and five (sixth transition) water molecules. Results obtained through six independent sets of umbrella

sampling (US) simulations using a similar collective variable (CV, see figure inset) as in Ref. 33. Additional US simulations are reported in Supplementary Section S9.3.

Fig. 5 **| Generalisation of the design rules. a**, Energy absorption densities of various hydrophobic cage-type ZIFs as a function of the strain rate. The error bars represent the uncertainty due to the incomplete unloading curves. **b**, Water intrusion and extrusion of ZIF-71 at three different strain rates, which correspond to a specific volume change rate $\Delta\dot{V}$ of 1×10^{-4}, 1×10^{-1}, and 80 $cm^3\,g^{-1}\,s^{-1}$, respectively. **c**, Water intrusion of ZIF-7 and ZIF-9 at three different strain rates, which correspond to $\Delta\dot{V}$ of 1×10^{-4}, 1×10^{-2}, and 1 $cm^3\,g^{-1}\,s^{-1}$, respectively. Their intrusion pressures, which can be identified from the $\Delta P/\Delta\varepsilon$ during loading process (inset), increase with the strain rate as design rule #2 is satisfied, although design rule #3 is violated. **d**, Water intrusion and extrusion of ZIF-8 and ZIF-67 at three different strain rates, which correspond to $\Delta\dot{V}$ of 1×10^{-2}, 70, and 7×10^{3} $cm^3\,g^{-1}\,s^{-1}$, respectively. Plots in **c** and **d** are offset horizontally for clarity. **e**, Materials selection map of the 105 ZIFs tabulated in Ref. 34 and Supplementary Section S10 according to their PLD and LCD, showing 20 promising materials fulfilling our design rules (□ to ■); others are either not hydrophobic (as determined by their linkers, ○), not cage-type (△), or have too small a PLD (◇). Experimentally validated materials are bold-faced (☆).

Fig. 6 | Water intrusion and extrusion of channel-containing zeolites at different conditions. a, Water intrusion pressure as a function of strain rate, comparing the behaviour of channel-containing zeolites against cage-type ZIFs. Due to the limited pore volume of mordenite, its intrusion pressure at higher loading rate is not available. **b**, Water intrusion and extrusion of ZSM-5 at three different strain rates, which correspond to a specific volume change rate $\Delta\dot{V}$ of 2×10^{-3}, 20, and 2×10^{3} $cm^3\,g^{-1}\,s^{-1}$, respectively. **c**, Comparison between ZIF-8 and ZSM-5 under high-rate deformation. **d,** Intrusion pressure, extrusion pressure, and energy absorption density of ZSM-5 (dark colour and filled symbols) at the three different conditions, compared with ZIF-8 (light colour and open symbols). The error bars represent the uncertainty due to the incomplete unloading curves at high strain rates.

Methods

Material synthesis and characterisation. ZIF-8 was purchased from Aldrich Sigma (Basolite® Z1200). Other ZIFs were synthesized using chemical compounds without further purification following the protocols outlined in Supplementary Section S1.2. Zeolites ZSM-5, zeolite-β, and mordenite were purchased from Alfa Aesar (45883, 45875, 45877 respectively). All of them were heated at 1,000 °C for 3 h and cooled in air, in order to obtain higher hydrophobicity before use. The chabazite was obtained from Johnson-Matthey (1318-02-1 22:1 CHA) and was heated at 950 °C for 3 h before use. This heat treatment procedure can increase the Si/Al ratio through dealumination, and therefore has been established as an efficient way to enhance the hydrophobicity of zeolites.[41,42] The effect of different heat treatment conditions on their water intrusion behaviours is shown in Supplementary Section S11.6. Microscopy imaging and X-ray diffraction of the synthesized samples were performed, and results are shown in Supplementary Section S1.3-14 and S2.6.

Sample fabrication. The obtained ZIFs and deionized water were combined and sealed in a stainless-steel chamber by precisely-fitting sealing rings. As shown in Fig. 1, the thickness of the sample is always 3 mm. In the low-rate Instron experiments and medium-rate hydraulic experiments, we adjusted the diameter of the sample to 6 mm, which includes 25 mg of ZIF material. In the SHPB experiments, we scaled the sample up to 12.7 mm in diameter, which includes 112 mg of ZIF material. As such, the pistons of the sealing chamber have the same diameter as the bars of SHPB, which means they can be impedance matched to avoid reflection of stress waves at the piston-bar interface.

Because of the relatively lower pore volume of zeolites compared to ZIFs, a higher amount of zeolites was used per sample, so that the lengths of water intrusion and extrusion plateaus are comparable to those of the ZIFs. This allows better identification of the corresponding pressures from the pressure-volume curves. Using a different amount of zeolites does not affect our observations, as shown in Supplementary Section S11.5. To fabricate a sample of 6 mm in diameter, we adopted 100 mg for ZSM-5, 50 mg for zeolite-β, and 50 mg for mordenite. For the larger sample, 12.7 mm in diameter, we used 448 mg for ZSM-5, 224 mg for zeolite-β, and 224 mg for mordenite.

Liquid intrusion experiments. Our liquid intrusion experimental platform is shown in Fig. 1. It is composed of a sealing chamber of the sample (Fig. 1c) and three different mechanical loading apparatus that provide appropriate driving force for water intrusion at different loading rates and allow the corresponding stress-strain measurement. The loading apparatus includes a commercial screw-driven load frame (Instron 5582) for low-rate experiments (up to 0.1 s^{-1}), an in-house hydraulic compression machine for medium-rate experiments (1-10^2 s^{-1}), and the Split-Hopkinson-Pressure-Bar (SHPB) setup for high-rate experiments (10^3 s^{-1}). By employing this experimental platform, pressure-volume change (P-ΔV) curves or stress-strain curves along the water intrusion and extrusion process are obtained over a wide range of strain rates (10^{-5}-10^3 s^{-1}).

The efficacy of the low-rate experimental method has been reported in our recent work.[12,18] We applied a constant crosshead displacement rate, corresponding to a certain strain rate in the sample. Then, at a peak pressure at which water molecules have filled the framework porosity (*e.g.*, 56 MPa for ZIF-8), we reversed the crosshead direction to obtain the extrusion behaviour at the same displacement rate. The Instron records the force and displacement history during the loading and unloading cycles.

Medium-rate experiments were conducted on a hydraulic compression machine (Fig. 1b), consisting of a hydraulic actuator, a strain-gauge based force transducer, and a pair of linear variable differential transformers (LVDTs) for displacement measurement. An appropriate peak displacement is pre-set, at which water molecules have filled up the framework porosity. We used the same strain rate for the loading and unloading process, which is controlled by the hydraulic actuator and measured by the displacement signals from the LVDTs.

High-rate experiments were carried out on a SHPB setup driven by a gas gun. In the experiment, the impact of a striker onto the incident bar produces an incident stress wave which propagates through the sample, with a certain amount being reflected, into the transmitted bar. The wave profiles recorded by the strain gauges on the incident and transmitted bars are used to calculate the forces and displacements at the specimen-bar interfaces and hence produce stress-strain curves using standard calculations.[43] The strain rate was also recorded using the reflected wave throughout the loading and unloading process. Stress equilibrium inside the sample during the impact is checked for each experiment, by confirming that the forces at the two interfaces have the same magnitude. All bars, including the piston of the sealing chamber, are made of the same material and have the same diameter, so as to match the impedances. Tungsten is selected as the bar material, to provide sufficient impact energy to drive the water intrusion process and allowing us to obtain experimental data at higher strain rates. Pulse shapers are employed to achieve a constant strain rate during the loading process. The unloading process of the sample is uncontrolled, which means that the strain rate during the unloading process is not constant and can be different from that of the loading process. The unloading data were recorded and used to reveal the intrinsic extrusion behaviour of water from the nanoporous framework. This procedure is different from the low-rate and medium-rate experiments, where the unloading process is still displacement-controlled by the compression head and the unloading rate is set to be the same as the loading rate. Unfortunately, without any driving force, the SHPB technique does not allow us to capture a complete unloading curve, unless extremely long bars are used, which are not available. The uncontrolled free water extrusion process in high-rate experiments represents the performance of {ZIF+water} systems under realistic impact loading conditions, and the difference in the unloading setting for experiments at different strain rates does not affect our discussion on the rate-dependent energy absorption phenomenon (see Supplementary Section S2.1).

Based on the obtained P-ΔV or stress-strain curves, the intrusion pressure P_{in} is determined as the onset of the intrusion plateau, while the extrusion pressure P_{ex} is determined as the midpoint of the extrusion plateau. For the incomplete extrusion plateaus in high-rate experiments, P_{ex} is taken from the last data point. The plateaus of ZIF-7, ZIF-9, and mordenite are short; therefore, their P_{in} and P_{ex} are determined based on the gradient of the plot. The intrusion and extrusion rates are taken from the value of the selected data point of P_{in} and P_{ex}. The strain rate history during the intrusion and extrusion is perfectly constant in

the low-rate experiments but has some oscillations in the medium-rate and high-rate experiments. Energy absorption is defined as the hysteresis area enclosed by the loading and unloading curve, which is a certain percentage of the mechanical energy stored during the loading process.

Periodic *ab initio* simulations. 0 K density functional theory (DFT) calculations were performed with the Vienna Ab initio Simulation Package (VASP)[44] using the projector-augmented wave (PAW) method.[45] The computational unit cell contained a total of 276 atoms, 12 of which are zinc atoms. The PBE exchange-correlation functional[46] was combined with the DFT-D3 dispersion scheme using Becke-Johnson damping.[47,48] The recommended GW PBE PAW potentials were employed for all elements and functionals (v5.4). For the zinc atoms, the 3s, 3p, 3d, and 4s electrons were included explicitly. For the carbon and nitrogen atoms, the 2s and 2p electrons were considered as valence electrons. For the hydrogen atoms, the 1s electron was treated as a valence electron. These DFT calculations were performed with a plane-wave kinetic-energy cut-off of 800 eV and using Gaussian smearing with a smearing width of 0.05 eV. Projection operators were evaluated in reciprocal space. A Γ-point k-grid was used for all volumes. The real-space FFT grid was used to describe wave vectors up to two times the maximum wave vector present in the basis set. An augmentation grid that is twice as large was used to avoid wrap-around errors in order to obtain accurate forces. The electronic (ionic) convergence criterion was set to 10^{-9} (10^{-8}) eV. The resulting energy equation of state, reported in Supplementary Section S3.1, was constructed by fixed volume relaxations in which the positions and cell shape were optimized.[49] Subsequently, the dynamical matrix was determined using 0.015 Å displacements for all atomic coordinates with respect to the equilibrium structure.

To probe the influence of temperature on the ZIF-8 swing angle, an additional set of $(N, P, \boldsymbol{\sigma}_a = \mathbf{0}, T)$ *ab initio* MD simulations[50] was performed at temperatures of 100 K, 200 K, and 300 K and at 0 MPa using the CP2K software package.[51,52] In these calculations, the PBE-D3(BJ)[46-48] level of theory was used in combination with Gaussian TZVP-MOLOPT basis sets,[53] a plane wave basis set with a cut-off of 800 Ry and a relative cut-off of 60 Ry, and Goedecker-Teter-Hutter (GTH) pseudopotentials.[54] The temperature of the simulations was controlled with a Nosé-Hoover chain thermostat consisting of three beads and with a time constant of 0.1 ps.[55-58] The pressure was controlled with a Martyna-Tobias-Klein barostat with a time constant of 1 ps.[59,60] These parameters were validated before to correctly capture the flexibility of MOFs.[50] The MD time step was set to 0.5 fs. The total simulation time for the AIMD simulations comprised 11 ps, of which the first ps was discarded for equilibration.

Force field derivation. From the dynamical matrix determined above, a flexible and *ab initio*-based force field for the empty ZIF-8 structure was derived. The covalent part of the force field, which contains diagonal terms that describe bonds, bends, out-of-plane distances, and torsion angles, as well as cross terms was derived using the in-house QuickFF software package.[61,62] The Lennard-Jones parameters were obtained from the Dreiding force field,[63] whereas the electrostatics were modelled as Coulomb interactions between Gaussian charge distributions[64] with the atomic charges computed using the Minimal Basis Iterative

Stockholder (MBIS) partitioning method.[65] More details about the ZIF-8 force field derivation are provided in Supplementary Section S3.2.

To describe the interactions between the different adsorbed water molecules and between the water molecules and the framework, a Lennard-Jones potential and point-charge electrostatics were used. The water molecules were described with the TIP4P/2005f model.[27] This model was chosen given its agreement with experimental water adsorption isotherms,[16,28,29] although the rigid TIP4P/2005 model does underestimate the vapor pressure.[66]

Force field based Monte Carlo simulations. Canonical Monte Carlo (MC) and grand canonical Monte Carlo (GCMC) simulations were performed using the RASPA2 software package[67] to extract the water density plots in the ZIF-8 framework. To this end, we first performed a series of GCMC simulations at a temperature of 298 K and a water pressure that varied from 300 Pa to 6.6 kPa over the different simulations, using the Peng-Robinson equation of state to relate the water pressure and the chemical potential.[68] From these GCMC results, the saturation limit was determined and initial {ZIF-8+water} snapshots were extracted at water loadings of 4, 8, 20, 40, 60, and 80 water molecules. These snapshots were then used as the starting point for separate canonical MC simulations, in which the water loading was kept constant and at a temperature of 298 K. In these canonical MC simulations, the average density of the centres of mass of the water molecules was averaged over at least 2 million MC cycles. The framework structures for the open- and closed-gate configurations of ZIF-8 were obtained from Ref. 31 (identifiers TUDHUW and TUDJOS in the Cambridge Crystallographic Database for the AP and HP phases, respectively) and the simulations were performed in a 2×2×2 supercell. During these MC simulations, the framework and the internal coordinates of the water molecules were kept rigid. The Lennard-Jones interactions were truncated at 12 Å with analytical tail-corrections to correct for the finite cut-off. Electrostatic interactions were treated using the Ewald summation method.[69]

Force field based molecular dynamics simulations. Based on the GCMC determined saturation limit of 80 water molecules per unit cell, 21 initial ZIF-8 structures were generated with 0, 4 ,8, …, 80 water molecules per unit cell by varying the chemical potential during the GCMC simulations. To create an inhomogeneous water distribution, the initial structure with 80 water molecules was doubled along one of the crystal axes, and all water molecules except for those in one out of four cages were removed (see Fig. 4). For each water loading, 11 simulations were run at pressures spaced equally between 0 MPa and 100 MPa.

For each of these structures and pressures, an $(N, P, \boldsymbol{\sigma_a} = \mathbf{0}, T)$ MD simulation[50] has been performed using our in-house developed software code Yaff[70] for a total simulation time of 3 ns (inhomogeneous water distribution) or 5 ns (homogeneous water distribution). Furthermore, for the longer simulations and the larger ZIF-8 models discussed in Supplementary Section S8, the Yaff software package was interfaced with LAMMPS to calculate the long-range interactions more efficiently.[71] During these $(N, P, \boldsymbol{\sigma_a} = \mathbf{0}, T)$ MD simulations, the temperature was controlled to be on average 300 K using a Nosé-Hoover chain thermostat consisting of three beads and with a time constant of 0.1 ps.[55-58] The pressure was controlled with a Martyna-Tobias-Klein barostat with a time constant of 1 ps.[59,60] The integration time step was limited to 0.5 fs to ensure energy conservation

when using the velocity Verlet scheme. The long-range van der Waals interactions were cut off at a radius of 12 Å, which was compensated by tail corrections. The electrostatic interactions were efficiently calculated using an Ewald summation with a real-space cut-off of 12 Å, a splitting parameter α of 0.213 $Å^{-1}$, and a reciprocal space cut-off of 0.32 $Å^{-1}$.[69] The snapshots in Fig. 4c were generated using VMD,[72] while the pore limiting diameter and largest cavity diameters were calculated with Zeo++.[73]

Force field based umbrella sampling simulations. To quantify the free energy associated with the hopping of a water molecule from one cage to an adjacent cage in ZIF-8, umbrella sampling (US) simulations were performed using our in-house developed software code Yaff.[70,74] A 2x2x2 ZIF-8 supercell was adopted to avoid potential, spurious interactions between periodic images of the water molecules. From the 16 cages in this supercell, 14 cages were kept empty, leaving only two adjacent cages that were potentially filled, named cage 1 and cage 2. The collective variable (CV) used in these US simulations is based on earlier diffusion work in related zeolite materials and is defined as follows.[33] First, the relative vector between the centroid of the selected water molecule that undergoes the hopping and the centre of the 6MR aperture separating cages 1 and 2 is determined. The CV is then defined as the oriented, perpendicular projection of this relative vector on the outwards normal of this 6MR aperture as observed from cage 1. Hence, CV = 0 Å corresponds to the water molecule being in the 6MR aperture, while CV < 0 Å and CV > 0 Å correspond to the molecule being in cage 1 and 2, respectively.

For each of the twenty different transitions (*vide infra*), the collective variable was divided into 47 equidistant windows centred with CV values between -11.5 Å and 11.5 Å. To restrict the simulation to each individual window, a harmonic bias potential at the centres of these equidistant windows was applied with a force constant of 25 kJ mol^{-1} $Å^{-2}$. Each of these US simulations was run for 2.25 ns, including 10 ps equilibration time. After this, the free energy profile for each of the transitions was obtained from the sampling distribution in each window by the weighted histogram analysis method (WHAM).[75,76] To prevent the other water molecules from escaping from their respective cages, an additional harmonic bias potential with a force constant of 100 kJ mol^{-1} $Å^{-2}$ was applied to each of those other water molecules whenever the centroid of the molecule was at least at a distance of 9 Å from the respective cage centre; this bias potential disappeared as long as the water molecules remained within a radius of 9 Å from their respective cage centres. This bias was also applied to the water molecule that undergoes the transition, but only when the molecule was sufficiently far from the 6MR aperture and hence sufficiently committed to one cage ($|CV| \geq 3$ Å). In this case, the additional spherical bias, which adds to the harmonic bias defined by the umbrella sampling, does not influence the transition through the 6MR aperture that is used in the definition of the CV, but prevents the water molecule from leaving the cage through a different 6MR aperture, similar to the effect of the spherical bias on the spectator water molecules.

The above procedure was followed for twenty different transitions. In the first set of ten transitions, besides the biased water molecule, cage 1 was filled with a critical cluster of five water molecules, while cage 2 was filled with in between zero (first transition) and nine (tenth transition) water molecules. The results of the first six of these simulations are shown in Fig. 4d. In the second set of ten transitions, this procedure was repeated but with a supercritical cluster of thirty molecules instead of a

critical cluster of five water molecules in cage 1 to quantify the effect of supersaturation. All results are discussed in Supplementary Section S9.3.

Data availability. The experimental dataset generated during the current study are available from the authors upon reasonable request. Relevant configurations for the optimizations and molecular dynamics simulations are available through Zenodo.[77] Additional computational data supporting the results of this work are available from the online GitHub repository at https://github.com/SvenRogge/supporting-info or upon request from the authors.

Code availability. The Yaff software used to perform the MD simulations in this manuscript is freely accessible via https://molmod.ugent.be/software/yaff. Representative input and processing scripts are available at https://github.com/SvenRogge/supporting-info.

References

41. Sun, Y. *et al.* Experimental study on energy dissipation characteristics of ZSM-5 zeolite/water system. *Adv. Eng. Mater.* **15**, 740-746 (2013).
42. Sun, Y. *et al.* A candidate of mechanical energy mitigation system: Dynamic and quasi-static behaviors and mechanisms of zeolite β/water system. *Mater. Des.* **66**, 545-551 (2015).
43. Gray, G. T., III. Classic split hopkinson pressure bar testing. *ASM Handbook* **8**, 462-476 (2000).
44. Kresse, G. & Furthmüller, J. Efficient iterative schemes for ab initio total-energy calculations using a plane-wave basis set. *Phys. Rev. B* **54**, 11169-11186 (1996).
45. Kresse, G. & Joubert, D. From ultrasoft pseudopotentials to the projector augmented-wave method. *Phys. Rev. B* **59**, 1758-1775 (1999).
46. Perdew, J. P., Burke, K. & Ernzerhof, M. Generalized gradient approximation made simple. *Phys. Rev. Lett.* **77**, 3865-3868 (1996).
47. Grimme, S., Antony, J., Ehrlich, S. & Krieg, H. A consistent and accurate ab initio parametrization of density functional dispersion correction (DFT-D) for the 94 elements H-Pu. *J. Chem. Phys.* **132**, 154104 (2010).
48. Grimme, S., Ehrlich, S. & Goerigk, L. Effect of the damping function in dispersion corrected density functional theory. *J. Comput. Chem.* **32**, 1456-1465 (2011).
49. Vanpoucke, D. E. P., Lejaeghere, K., Van Speybroeck, V., Waroquier, M. & Ghysels, A. Mechanical properties from periodic plane wave quantum mechanical codes: The challenge of the flexible nanoporous MIL-47(V) framework. *J. Phys. Chem. C* **119**, 23752-23766 (2015).
50. Rogge, S. M. J. *et al.* A comparison of barostats for the mechanical characterization of metal-organic frameworks. *J. Chem. Theory Comput.* **11**, 5583-5597 (2015).
51. VandeVondele, J. *et al.* Quickstep: Fast and accurate density functional calculations using a mixed Gaussian and plane waves approach. *Comput. Phys. Commun.* **167**, 103-128 (2005).
52. Hutter, J., Iannuzzi, M., Schiffmann, F. & VandeVondele, J. CP2K: atomistic simulations of condensed matter systems. *Wiley Interdiscip. Rev. Comput. Mol. Sci.* **4**, 15-25 (2014).
53. VandeVondele, J. & Hutter, J. Gaussian basis sets for accurate calculations on molecular systems in gas and condensed phases. *J. Chem. Phys.* **127**, 114105 (2007).
54. Goedecker, S., Teter, M. & Hutter, J. Separable dual-space Gaussian pseudopotentials. *Phys. Rev. B* **54**, 1703-1710 (1996).
55. Nosé, S. A molecular dynamics method for simulations in the canonical ensemble. *Mol. Phys.* **52**, 255-268 (1984).
56. Nosé, S. A unified formulation of the constant temperature molecular dynamics methods. *J. Chem. Phys.* **81**, 511-519 (1984).
57. Hoover, W. G. Canonical dynamics: Equilibrium phase-space distributions. *Phys. Rev. A* **31**, 1695-1697 (1985).
58. Martyna, G. J., Klein, M. L. & Tuckerman, M. Nosé–Hoover chains: The canonical ensemble via continuous dynamics. *J. Chem. Phys.* **97**, 2635-2643 (1992).
59. Martyna, G. J., Tobias, D. J. & Klein, M. L. Constant pressure molecular dynamics algorithms. *J. Chem. Phys.* **101**, 4177-4189 (1994).
60. Martyna, G. J., Tuckerman, M. E., Tobias, D. J. & Klein, M. L. Explicit reversible integrators for extended systems dynamics. *Mol. Phys.* **87**, 1117-1157 (1996).
61. Vanduyfhuys, L. *et al.* Extension of the QuickFF force field protocol for an improved accuracy of structural, vibrational, mechanical and thermal properties of metal-organic frameworks. *J. Comput. Chem.* **39**, 999-1011 (2018).
62. Vanduyfhuys, L. *et al.* QuickFF: A program for a quick and easy derivation of force fields for metal-organic frameworks from ab initio input. *J. Comput. Chem.* **36**, 1015-1027 (2015).
63. Mayo, S. L., Olafson, B. D. & Goddard, W. A. DREIDING: a generic force field for molecular simulations. *J. Phys. Chem.* **94**, 8897-8909 (1990).
64. Chen, J. & Martínez, T. J. QTPIE: Charge transfer with polarization current equalization. A fluctuating charge model with correct asymptotics. *Chem. Phys. Lett.* **438**, 315-320 (2007).
65. Verstraelen, T. *et al.* Minimal basis iterative stockholder: Atoms in molecules for force-field development. *J. Chem. Theory Comput.* **12**, 3894-3912 (2016).
66. Chen, J. L., Xue, B., Mahesh, K. & Siepmann, J. I. Molecular Simulations Probing the Thermophysical Properties of Homogeneously Stretched and Bubbly Water Systems. *J. Chem. Eng. Data* **64**, 3755-3771 (2019).
67. Dubbeldam, D., Calero, S., Ellis, D. E. & Snurr, R. Q. RASPA: molecular simulation software for adsorption and diffusion in flexible nanoporous materials. *Mol. Simul.* **42**, 81-101 (2015).

68. Peng, D.-Y. & Robinson, D. B. A new two-constant equation of state. *Ind. Eng. Chem. Fundam.* **15**, 59-64 (1976).
69. Ewald, P. P. Die Berechnung optischer und elektrostatischer Gitterpotentiale. *Ann. der Phys.* **369**, 253-287 (1921).
70. Yaff, yet another force field. Available online at http://molmod.ugent.be/software/.
71. Plimpton, S. Fast parallel algorithms for short-range molecular dynamics. *J. Comput. Phys.* **117**, 1-19 (1995).
72. Humphrey, W., Dalke, A. & Schulten, K. VMD: Visual molecular dynamics. *J. Mol. Graph.* **14**, 33-38 (1996).
73. Willems, T. F., Rycroft, C. H., Kazi, M., Meza, J. C. & Haranczyk, M. Algorithms and tools for high-throughput geometry-based analysis of crystalline porous materials. *Microporous Mesoporous Mat.* **149**, 134-141 (2012).
74. Torrie, G. M. & Valleau, J. P. Nonphysical sampling distributions in Monte Carlo free-energy estimation: Umbrella sampling. *J. Comput. Phys.* **23**, 187-199 (1977).
75. Kumar, S., Rosenberg, J. M., Bouzida, D., Swendsen, R. H. & Kollman, P. A. The weighted histogram analysis method for free-energy calculations on biomolecules. I. The method. *J. Comput. Chem.* **13**, 1011-1021 (1992).
76. Souaille, M. & Roux, B. Extension to the weighted histogram analysis method: combining umbrella sampling with free energy calculations. *Comput. Phys. Commun.* **135**, 40-57 (2001).
77. Rogge, S. M. J. Supporting molecular data for High rate nanofluidic energy absorption in porous zeolitic frameworks. (2021). doi: 10.5281/zenodo.4534252